

Uncovering the Edge of the Polar Vortex

MATTIA SERRA^a

Institute for Mechanical Systems, Eidgenössische Technische Hochschule Zürich, Zurich, Switzerland

PRATIK SATHE

Department of Physics, Indian Institute of Technology Bombay, Mumbai, India

FRANCISCO BERON-VERA

Rosenstiel School of Marine and Atmospheric Science, University of Miami, Miami, Florida

GEORGE HALLER

Institute for Mechanical Systems, Eidgenössische Technische Hochschule Zürich, Zurich, Switzerland

(Manuscript received 18 February 2017, in final form 13 July 2017)

ABSTRACT

The polar vortices play a crucial role in the formation of the ozone hole and can cause severe weather anomalies. Their boundaries, known as the vortex “edges,” are typically identified via methods that are either frame dependent or return nonmaterial structures and, hence, are unsuitable for assessing material transport barriers. Using two-dimensional velocity data on isentropic surfaces in the Northern Hemisphere, the authors show that elliptic Lagrangian coherent structures (LCSs) identify the correct outermost material surface dividing the coherent stratospheric vortex core from the surrounding incoherent surf zone. Despite the purely kinematic construction of LCSs, the authors find a remarkable contrast in temperature and ozone concentration across the identified vortex boundary. The authors also show that potential vorticity-based methods, despite their simplicity, misidentify the correct extent of the vortex edge.

1. Introduction

The formation, deformation, and breakdown of the polar vortices play an influential role in stratospheric circulation, in both the Northern and Southern Hemispheres. The beginning of winter is characterized by a rise in circumpolar wind velocities in the stratosphere, resulting in a vortical motion delineated by a transport barrier that isolates polar air from tropical and midlatitude stratospheric air. This coherent air mass is commonly referred to as the main vortex, while its enclosing barrier is known as the vortex “edge” (Mizuta and Yoden 2001; Nash et al. 1996).

The spatial extent and strength of the vortex edge determine the severity, location, and size of the ozone hole in the stratosphere (World Meteorological Organization 1992;

McIntyre 1995; Schoeberl and Hartmann 1991; Shepherd 2007), which is more prominent in the Southern Hemisphere. The chemical composition of the polar stratospheric air differs significantly from the midlatitudinal air (Leovy et al. 1985; Krueger et al. 1989; Loewenstein et al. 1989; Russell et al. 1993), and the dynamics of the polar vortex profoundly affect such composition (Olascoaga et al. 2012; Huck et al. 2005; Hood and Soukharev 2005). The chemical isolation and low temperatures inside the polar vortex are necessary for the formation of polar stratospheric clouds (PSCs), the main factor responsible for the rapid stratospheric ozone loss during spring.

The material deformation of the vortex edge also exerts a major influence on Earth’s surface weather (Mitchell et al. 2013). Although both stratospheric and tropospheric polar vortices influence surface weather, implications on surface weather due to the stratospheric polar vortex deformation are more subtle and indirect (Vaugh et al. 2016). Except during vortex break-off events, the cold air in the vortex interior remains well

^a Current affiliation: Paulson School of Engineering and Applied Sciences, Harvard University, Cambridge, Massachusetts.

Corresponding author: Mattia Serra, serram@seas.harvard.edu

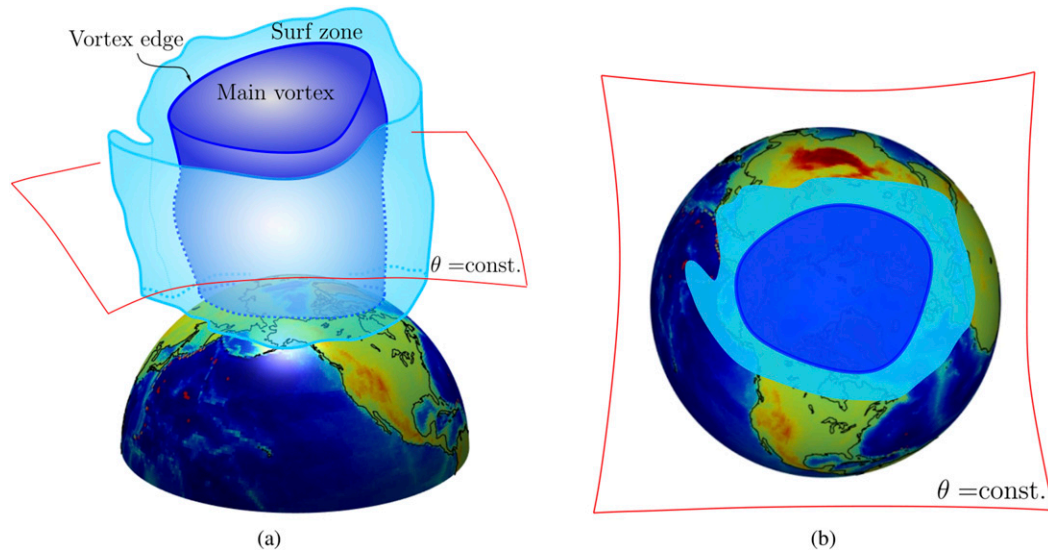


FIG. 1. (a) Sketch of the polar vortex and its two dynamically distinct regions: the coherent main vortex enclosed by the vortex edge and the incoherent surrounding surf zone. The main vortex retains cold air while the highly mixed surf zone sheds filaments of warmer air to lower latitudes. (b) Cross section of the polar vortex on an isentropic surface ($\theta = \text{const.}$), where θ denotes the potential temperature.

isolated from its exterior (Schoeberl et al. 1989, 1992; Hartmann et al. 1989a,b; McIntyre 1989). Therefore, the exact spatial extent of the polar vortex edge and its material deformation are crucial for understanding the vortex dynamics and its impact on Earth's climate, ozone hole variability, and the composition of stratospheric air (Zhang et al. 2016).

Broadly used methods developed for locating the polar vortex edge agree that the polar vortex consists of two distinct regions: (i) the main vortex, which represents the coherent polar vortex core, and (ii) the surf zone, which is a wide surrounding incoherent region interacting with lower latitudes (cf. Fig. 1). Jukes and McIntyre write in their seminal paper Jukes and McIntyre (1987, p. 594), “remind us of the likely importance of considering the main vortex as a material entity or isolated airmass, for dynamical as well as chemical purposes.”

All this suggests the presence of a distinguished material surface confining the coherent evolution of the main vortex from the incoherent pattern of the surf zone. In geophysical flows, however, the most popular approaches to locating the vortex boundaries are Eulerian, returning nonmaterial structures based on nonmaterial coherence principles. In oceanic flows, for example, Eulerian diagnostic methods have been found to overestimate coherent material transport by an order of magnitude (Beron-Vera et al. 2013). We summarize these Eulerian approaches below.

From a meteorological perspective, heuristic methods for assessing the shape and movement of the polar vortex are based on the area diagnostic (Butchart and

Remsberg 1986; Baldwin and Holton 1988) and later extensions, termed elliptic diagnostics (Vaugh 1997; Vaugh and Randel 1999; Hannachi et al. 2011), which are mainly based on potential vorticity (PV). The vortex edge is then routinely identified by locating steep gradients of PV (McIntyre and Palmer 1984; Hood and Soukharev 2005; Nash et al. 1996; Steinhorst et al. 2005). Inspired by these heuristics, Nash et al. (1996) define the vortex edge as the closed PV contour with the highest gradient relative to the area it encloses. Other popular methods include effective diffusivity (Nakamura 1996; Haynes and Shuckburgh 2000; Hauchecorne et al. 2002; Allen and Nakamura 2001). From a chemical perspective, various other methods have been developed based on the chemical composition of the vortex interior (Harvey et al. 2015; McDonald and Smith 2013; Krützmann et al. 2008; Sparling 2000).

Lagrangian methods have also been used to locate the polar vortex edge. Bowman (1993) was the first to use the finite-time Lyapunov exponent (FTLE) for studying the Antarctic polar vortex. Beron-Vera et al. (2012) identify zonal jets in the lower stratosphere as transport barriers using locally minimizing curves of FTLE fields. Several other papers describe the connection between meridional transport barriers and stratospheric zonal jets (Beron-Vera et al. 2008; Olascoaga et al. 2012; Rypina et al. 2006; Beron-Vera et al. 2010) often based on identifying trenches of FTLE. De La Cámara et al. (2010) investigate the austral spring vortex breakup in 2005 based on high FTLE values, while Lekien and Ross (2010) develop FTLE computation technique over

non-Euclidean manifolds and use it to identify the 2002 Antarctic polar vortex breakup. Other methods are based on minimally stretching contours (Chen 1994; Norton 1994; Waugh and Plumb 1994). Koh and Legras (2002) compute the finite-size Lyapunov exponent (FSLE) field over 500-K isentropic data from the European Centre for Medium-Range Weather Forecasts (ECMWF) to identify transport barriers. Joseph and Legras (2002) conclude that high values of FSLE do not correctly identify the vortex boundary but rather delineate a highly mixed region outside the boundary called the “stochastic layer.” Other Lagrangian analyses are based on optimally coherent sets Santitissadeekorn et al. (2010) and trajectory length (Madrid and Mancho 2009; De La Cámara et al. 2012; Smith and McDonald 2014). Most of these methods, however, either lack objectivity (frame invariance) or identify nonmaterial structures. Furthermore, none of them give a rigorous parameter-free definition of the vortex edge but rather a visual indication of its approximate location through steep gradients of appropriate scalar fields.

Here, we apply the recently developed mathematical theory of geodesic Lagrangian coherent structures (LCSs) to locate the polar vortex edge. LCSs are distinguished surfaces in a dynamical system that invariably create coherent trajectory patterns over a finite time interval (Haller 2015). This kinematic (model independent) theory has already been applied to detect coherent structures in various atmospheric and oceanic flows (Farzmand et al. 2014; Haller and Beron-Vera 2013; Hadjighasem and Haller 2016; Karrasch et al. 2015; Serra and Haller 2017b). Specifically, elliptic LCSs are frame-independent distinguished material surfaces that attain exceptionally low deformation over a finite time interval (Haller 2015). This physical principle seems to be tailored precisely to identify the polar vortex edge described in the introduction and sketched in Fig. 1.

We compute elliptic LCSs on various isentropic surfaces in the northern midstratosphere in late December 2013 and early January 2014, when exceptionally cold weather was recorded in the northeastern United States. We show that a geodesic vortex boundary, defined as the outermost elliptic LCS around the polar vortex region, forms an optimal, nonfilamenting transport barrier dividing the vortex core from the surf zone and, hence, identifies the exact theoretical location of the polar vortex edge. We prove this optimality by materially advecting the geodesic vortex boundary along with a small perturbation to this boundary. Remarkably, we find the perturbed boundary undergoes significant deformations while the geodesic vortex boundary shows no filamentation.

We also find that in late December 2013, the polar vortex edge is initially centered and undeformed, while

in the early January 2014, it materially deforms toward the northeastern United States, consistently with the severe weather phenomena recorded over that time period. For a detailed description of the polar vortex influence on surface weather, see Waugh et al. (2016). The deformation of the polar vortex is typically visualized through the nonmaterial evolution of the PV field. We show, however, that the PV field misidentifies the correct extent of the vortex edge.

We briefly recap the theory of elliptic LCSs in section 2. In section 3, we describe the data and numerical methods. In section 4a, we show the vortex edge identified by elliptic LCSs. In sections 4b–e, we compare our results with the FTLE field, the vortex edge identified by PV-based methods, ozone concentration, and temperature fields.

2. Geodesic LCS theory

a. Setup and notation

Consider a two-dimensional unsteady velocity field:

$$\frac{dx}{dt} = v(x, t), \quad x \in U \subset \mathbb{R}^2, \quad t \in [t_0, t_1], \quad (1)$$

where U denotes a flow domain of interest. The trajectories of fluid elements define a flow map:

$$F_{t_0}^t(x_0) := x(t; t_0, x_0), \quad (2)$$

which takes every point x_0 at time t_0 to its position $F_{t_0}^t(x_0)$ at time t . The right Cauchy–Green strain tensor is often used to characterize Lagrangian strain generated by the flow map, defined as (Truesdell and Noll 2004)

$$\mathbf{C}_{t_0}^t(x_0) = [\nabla F_{t_0}^t(x_0)]^T \nabla F_{t_0}^t(x_0), \quad (3)$$

where $\nabla F_{t_0}^t$ is the gradient of the flow map and T denotes matrix transposition. The tensor $\mathbf{C}_{t_0}^t$ is symmetric and positive definite, with eigenvalues $0 < \lambda_1 \leq \lambda_2$ and an orthogonal eigenbasis $\{\xi_1, \xi_2\}$, which satisfy

$$\begin{aligned} \mathbf{C}_{t_0}^t(x_0) \xi_i(x_0) &= \lambda_i(x_0) \xi_i(x_0), \\ |\xi_i| &= 1, i = 1, 2; \quad \xi_2 = \begin{pmatrix} 0 & -1 \\ 1 & 0 \end{pmatrix} \xi_1. \end{aligned} \quad (4)$$

A common diagnostic for hyperbolic (i.e., attracting and repelling) LCSs in the flow is the FTLE field $\Lambda_{t_0}^t$ (Haller 2015), defined as

$$\Lambda_{t_0}^t(x_0) = \frac{1}{t - t_0} \log \sqrt{\lambda_2(x_0)}. \quad (5)$$

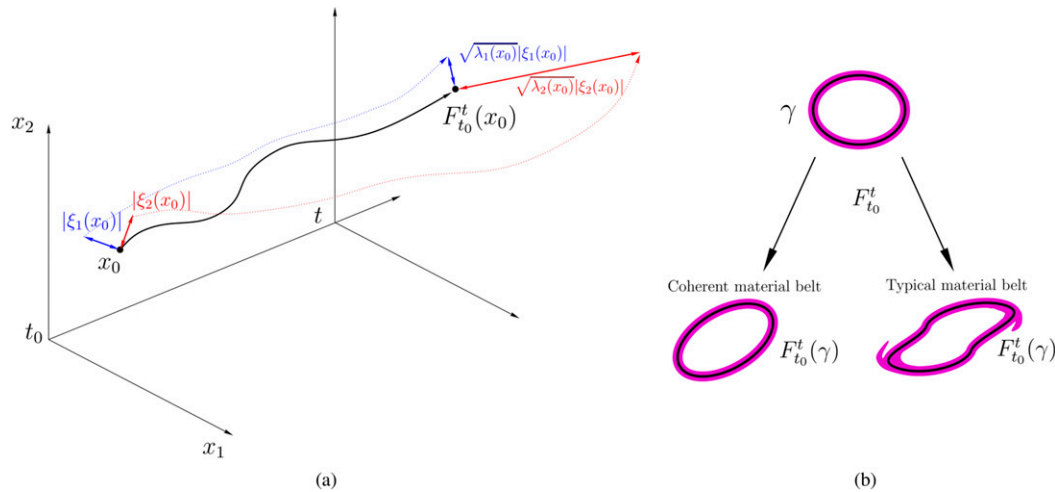


FIG. 2. (a) Evolution of fluid elements in a neighborhood of the initial point x_0 in the extended phase space of position and time, as described by Eqs. (2)–(4). (b) Material evolution of a typical closed material curve and of an elliptic LCS defined by Eq. (8).

The FTLE measures the maximum separation exponent of initially close particles over the time interval $[t_0, t]$. Its high values provide an intuitive idea of the location of most repelling material lines in the flow. The FTLE, however, does not carry information about the type of deformation causing particle separation, and hence, the underlying LCSs need further postprocessing to be identified reliably (Haller 2002). We illustrate Eqs. (2)–(5) in Fig. 2a.

A more precise variational approach classifies LCSs into three different types depending on the distinguished impact they have on nearby deformation patterns. Specifically, initial positions of hyperbolic LCSs (generalized stable and unstable manifolds), elliptic LCSs [generalized Kolmogorov–Arnold–Moser (KAM) tori] and parabolic LCSs (generalized jet cores) are computable as solutions of specific variational principles (Haller 2015; Serra and Haller 2017a). Later positions of these LCSs are then obtained by advecting their initial positions under the flow map. We now briefly recap the theory of elliptic LCSs used in this paper.

b. Elliptic LCSs

A typical set of fluid particles deforms significantly when advected under the flow map $F_{t_0}^t(\cdot)$. One may seek coherent material vortices as atypical sets of fluid trajectories that defy this trend by preserving their overall shape. These shapes should be bounded by closed material lines that rotate and translate but show no appreciable stretching or folding (cf. Fig. 2b). Motivated by this observation, Haller and Beron-Vera (2013) seek Lagrangian vortex boundaries as the outermost closed material lines across which the averaged material stretching shows no leading-order variability.

Mathematically, consider a closed smooth curve $\gamma \subset U$, parameterized in the form $x(s)$ by its arclength $s \in [0, \sigma]$. The averaged material strain along γ , computed between the times t_0 and t , is given by (Haller and Beron-Vera 2013):

$$Q = \frac{1}{\sigma} \int_0^\sigma \sqrt{\frac{\langle x'(s), \mathbf{C}_{t_0}^t[x(s)]x'(s) \rangle}{\langle x'(s), x'(s) \rangle}} ds, \tag{6}$$

where the angle brackets denote the Eulerian inner product and the prime denotes differentiation with respect to s . By the smoothness of the velocity field, $\mathcal{O}(\epsilon)$ perturbations to the material line γ will typically lead to $\mathcal{O}(\epsilon)$ variability in the averaged tangential stretching Q (Arnold 1973). Elliptic LCSs, in contrast, are sought as exceptional closed material lines whose $\mathcal{O}(\epsilon)$ perturbations show $\mathcal{O}(\epsilon)$ variability in the averaged tangential stretching (i.e., $\delta Q = 0$), as illustrated in Fig. 2b. This coherence principle models precisely the vortex edge sketched in Fig. 1.

Haller and Beron-Vera (2013) show that closed material lines γ satisfying $\delta Q(\gamma) = 0$ coincide with closed null geodesics of the Lorentzian metric:

$$g_{x_0, \lambda} := \langle x'_0, E_\lambda(x_0)x'_0 \rangle, \quad E_\lambda(x_0) = \frac{1}{2}[\mathbf{C}_{t_0}^t(x_0) - \lambda^2 I], \tag{7}$$

for some real constant λ . Adopting recently developed results for a fully automated computation of closed null geodesics (Serra and Haller 2017a), we compute the initial (time t_0) position of elliptic LCSs γ as the x projection of closed orbits of the initial-value-problem family:

$$x' = e_\phi := [\cos\phi, \sin\phi]^T,$$

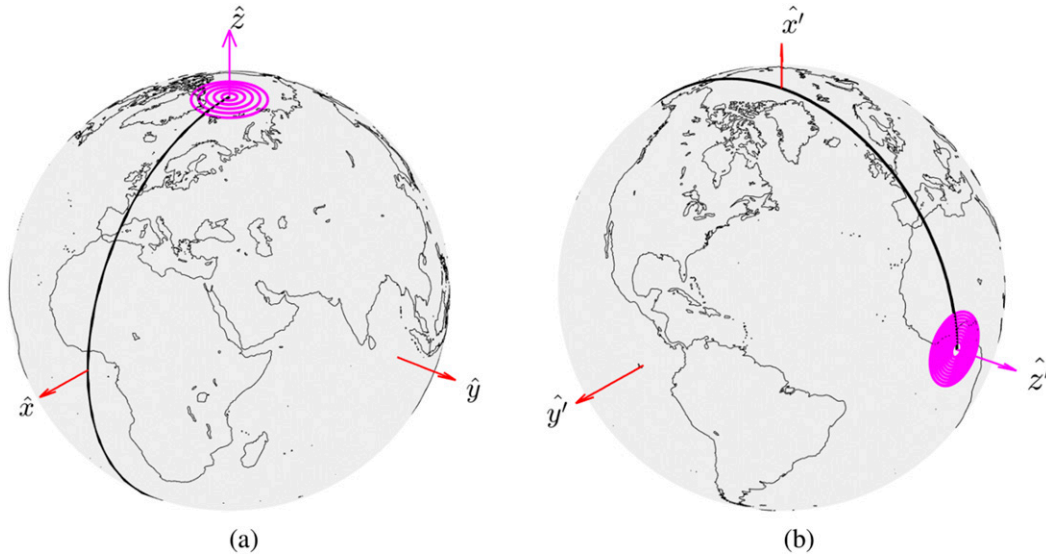


FIG. 3. (a) Original coordinate system. (b) New coordinate system suitable for Lagrangian analysis close to the North Pole. Magenta circles mark the computationally intractable region for trajectory calculations.

$$\phi' = -\frac{\cos^2\phi\langle\nabla_{x_0}C^{11}(x_0), e_\phi\rangle + \sin 2\phi\langle\nabla_{x_0}C^{12}(x_0), e_\phi\rangle + \sin^2\phi\langle\nabla_{x_0}C^{22}(x_0), e_\phi\rangle}{\sin 2\phi[C^{22}(x_0) - C^{11}(x_0)] + 2\cos 2\phi C^{12}(x_0)}, \quad (8)$$

$$x(0) = \{x \in U: C^{11}(x) - \lambda^2 = 0\}, \quad \phi(0) = 0.$$

Here, ϕ denotes the angle enclosed by the x' direction and the horizontal axis, and $C^{ij}(x_0)$ denotes the entry at row i and column j of the matrix $\mathbf{C}_{x_0}^i(x_0)$. Elliptic LCSs are closed curves whose arbitrarily small subsets stretch uniformly by the same factor of λ . The time t positions of these LCSs can be obtained by advecting their initial position under the flow map $F_{t_0}^i(\gamma)$. Geodesic vortex boundaries can then be identified as the outermost elliptic LCSs computed over a set of lambdas ranging from the weakly contracting ($\lambda < 1$) to the weakly stretching ($\lambda > 1$) curves. A MATLAB implementation of Eq. (8) is available in [Serra and Haller \(2017a\)](#).

3. Data and numerical methods

Synoptic-scale stratospheric mixing is quasi layer-wise and stratified; hence, most of the analyses are done on isentropic surfaces. For purely adiabatic flows, atmospheric motion is restricted to isentropic surfaces, an approximation that holds true over a period of 7–10 days in the stratosphere ([Morris et al. 1995, 2002](#)), consistently with the time interval considered in our analysis.

Using isentropic surface data from the ECMWF global reanalysis ([Dee et al. 2011](#)), we compute elliptic LCSs on the sequence of isentropic levels 850, 700, 600, 530, and 475 K using a range of λ values from 0.8 to 1.2 in 0.1 steps. The wind velocity and potential vorticity on each isentropic surface are available on a 0.75° latitude \times 0.75° longitude mesh grid, with a time resolution of 6 h. We focus on the time period from 28 December 2013 to 8 January 2014, when exceptionally severe cold weather affected the northeastern coast in the United States.

Our region of interest is the northern polar region. In a standard spherical coordinate system (cf. [Fig. 3a](#)), the zonal (longitudinal) wind velocity ($^\circ \text{ day}^{-1}$) tends to infinity at the North Pole, making trajectory calculations intractable in its vicinity. To this end, using a change of coordinates, we shift this singularity to a different location, far from the region we intend to analyze (cf. [Fig. 3b](#)).

We use cubic interpolation of the velocity field for trajectory integration and compute $\nabla F_{t_0}^i(x_0)$ according to [Haller \(2001\)](#). Specifically, we compute trajectories of four initial conditions (on an auxiliary grid) surrounding every point of the main grid, with the auxiliary grid size equal to 1% of the main grid size. We carry out the trajectory integration and the LCS calculations from Eq. (8) using ode45 in MATLAB, with absolute and relative tolerances set to 10^{-6} .

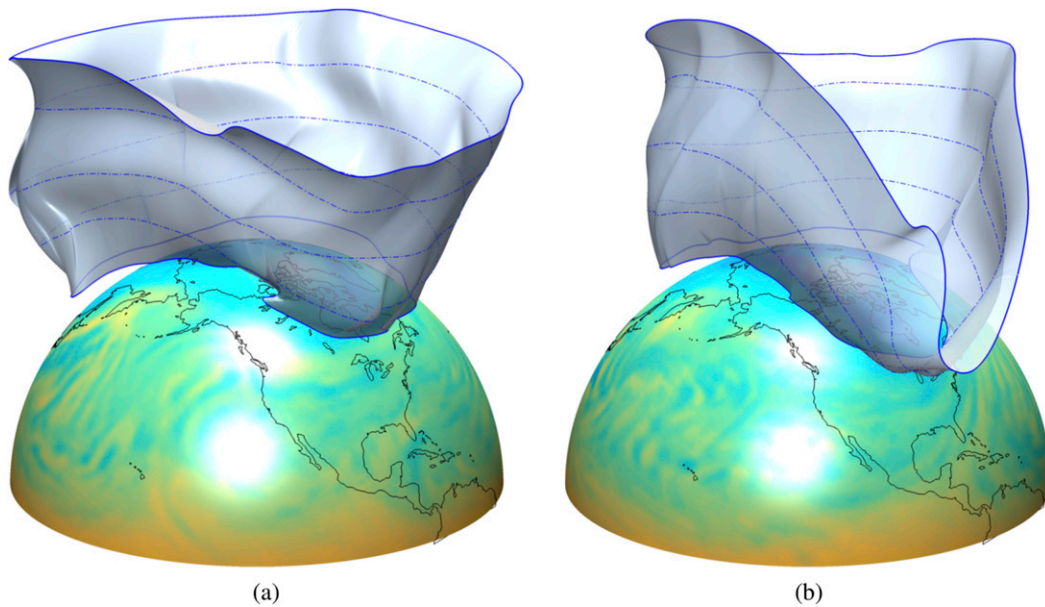


FIG. 4. Reconstructed 3D visualization of geodesic polar vortex edges obtained on all isentropic surfaces under consideration on (a) 28 Dec 2013 and (b) 7 Jan 2014. (Panels not to scale along the radial direction.) PV on the 475-K isentropic surface is plotted over Earth's surface. The full evolution on the vortex boundary over the 10-day time window is available (video 1: <https://goo.gl/7CQ9cu>).

4. Results

a. Elliptic LCSs identify the polar vortex edge

We perform a backward time analysis over a time interval $[t_0, t_1]$ of 10 days, with $t_0 = 7$ January 2014 and $t_1 = 28$ December 2013. From the positions of the outermost elliptic LCSs (i.e., geodesic vortex boundaries) on the five isentropic surfaces, we construct a three-dimensional (3D) visualization of the geodesic polar vortex edge spanning the middle and lower stratosphere (cf. Fig. 4). Such a 3D visualization enables us to make conclusions about the overall material deformation of the main vortex over the time interval we analyze. Specifically, Fig. 4a shows the vortex edge on 28 December 2013, which has an almost undeformed circular shape, while Fig. 4b shows the deformed vortex edge on 7 January 2014.

Note that the vortex edge deforms toward the northeastern coast of the United States, consistent with the exceptional cold recorded there over the early January 2014. A video showing the evolution of the 3D geodesic vortex edge over the 10-day time window is available (video 1: <https://goo.gl/7CQ9cu>).

OPTIMAL COHERENT TRANSPORT BARRIER

As noted in the introduction, the vortex edge is thought as the outermost closed material line dividing the main vortex from the surf zone. Here, we show the

optimality of the geodesic vortex boundary obtained as the outermost elliptic LCS. The optimal boundary of a coherent vortex can be defined as a closed material surface that encloses the largest possible area around the vortex and undergoes no filamentation over the observational time period. To this end, we consider a small normal perturbation to the geodesic vortex boundary. The amount of perturbation is 5° , that is, 10% of the equivalent diameter of the outermost elliptic LCSs. We then advect the geodesic vortex boundary and its perturbation over the time window under study.

As an illustration, Fig. 5a shows the initial positions of the geodesic vortex edge and its perturbation on the 600-K isentropic surface. Figures 5b–f, instead, show the advected images of the geodesic vortex and its perturbations on different isentropic surfaces. The geodesic vortex edge remains coherent under advection in all cases, in sharp contrast to the perturbations that undergo substantial filamentation over the 10-day time window.

Figure 6 shows a combined visualization of the initial positions of the geodesic vortex (blue) together with their perturbations (Fig. 6a) and their evolved positions (Fig. 6b) for all isentropic surfaces. A video showing the complete advection sequence over the 10-day time window is available (video 2: <https://goo.gl/7CQ9cu>).

The main vortex–surf zone distinction (McIntyre and Palmer 1983) divides the polar vortex into a coherent

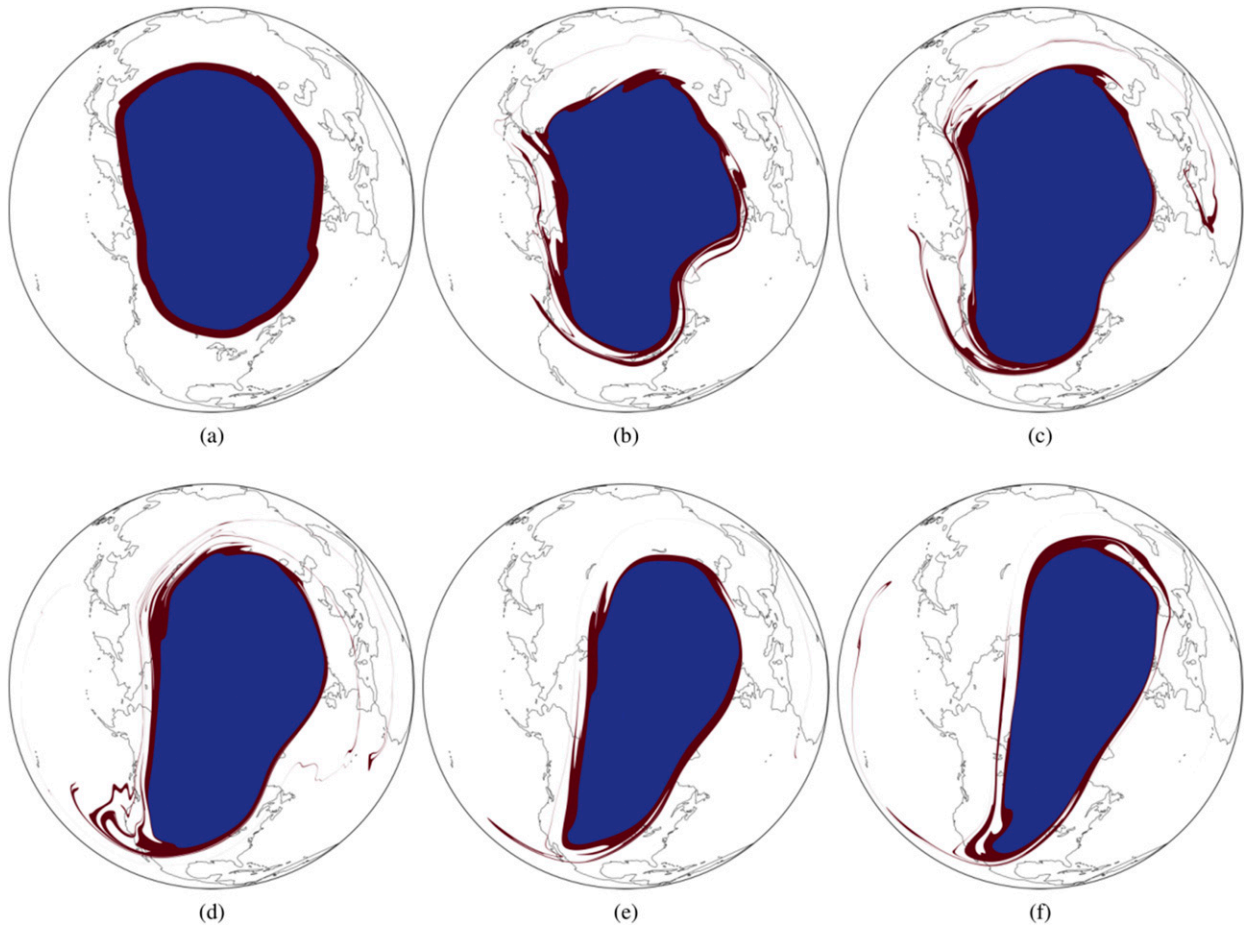


FIG. 5. (a) The position of the geodesic vortex edge (blue) on the 600-K isentropic surface on 28 Dec 2013, along with its outward perturbation (red). Also shown are advected images of the geodesic vortex edge and its perturbation on 7 Jan 2014 for the (b) 475-, (c) 530-, (d) 600-, (e) 700-, and (f) 850-K isentropic surfaces.

vortical air mass and its weakly coherent surrounding air, which gets eroded by planetary wave breaking. Thus, ideally, the polar vortex edge should enclose the coherent vortical air mass optimally. Such an optimality necessitates that the immediate exterior of the vortex edge, being a part of the surf zone, exhibit substantial advective mixing with the tropical air. This is because Rossby wave breaking irreversibly erodes the polar vortex, with long filaments of stratospheric air getting pulled off the surf zone and into the tropical regions (McIntyre and Palmer 1983, 1984). In Fig. 6, we observe precisely this behavior in the immediate vicinity of the geodesic vortex edge on each isentropic layer.

b. Elliptic LCS and PV-based methods

1) THE NASH METHOD

Here, we compare the geodesic polar vortex edge with the one obtained using the Nash method, that is, the PV

isoline possessing the maximum gradient of PV with respect to the equivalent latitude (Nash et al. 1996). PV contours are frequently used because in the idealized case of adiabatic and inviscid flows, isentropic PV is conserved, with strong PV gradients generating a restoring force inhibiting meridional transport (Vallis 2006). However, even under these idealistic assumptions, the vortex edge returned by the Nash method is frame dependent and nonmaterial, hence a priori unsuitable for a self-consistent detection of coherent transport barriers.

Despite our analysis being purely kinematic, we obtain an overall qualitative agreement between the geodesic vortex boundary and the ones obtained by the Nash method. However, the Nash method fails to capture the optimal vortex edge accurately, sometimes underestimating (Fig. 7a) and sometimes overestimating (Fig. 7b) it. The blue areas in Figs. 5b and 5e show the advected images of the geodesic vortices in

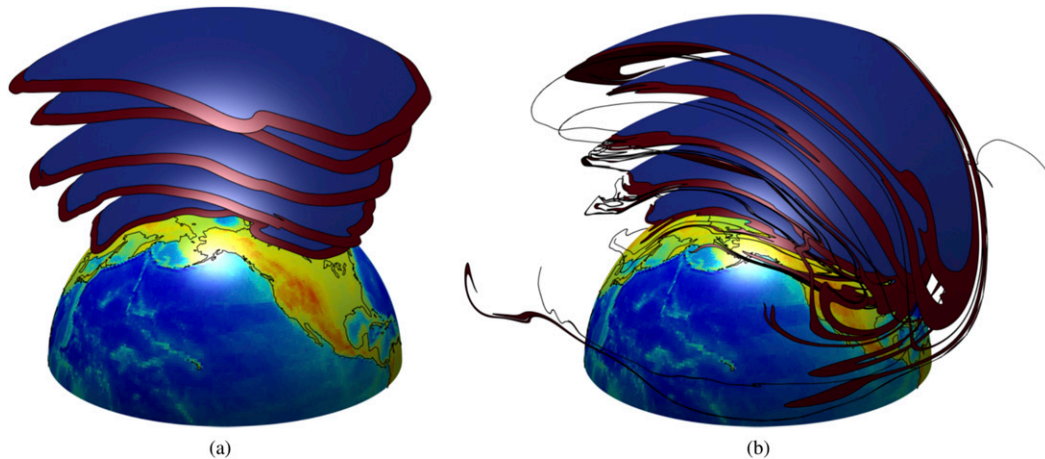


FIG. 6. (a) Geodesic vortex (blue) along with its perturbation (red) on 28 Dec 2013 on different isentropic surfaces. (b) Advected position of the geodesic vortex and its perturbation on 7 Jan 2014. (Panels not to scale along the radial direction.) This 3D visualization shows that the perturbation to the geodesic vortex edge undergoes substantial filamentation consistently across all isentropic surfaces. A video showing the complete advection sequence over the 10-day time window is available (video 2: <https://goo.gl/7CQ9cu>).

Figs. 7a and 7b. Invariably, these areas remain coherent without mixing with warmer air at lower latitudes, as opposed to their slight perturbations. This shows that the outermost materially coherent boundary can either enclose or be enclosed by the one indicated by the Nash method. Although PV generally decreases with increasing distance from the poles, often small pockets of high PV appear far away from the polar region. Hence, without further filtering, the

vortex edge identified by the Nash method could also include small patches of tropical air (cf. Fig. 7a).

Given its Eulerian (nonmaterial) nature, the Nash edge evolves discontinuously, with visible jumps in position and shape over time. In contrast, the geodesic vortex edge we extract evolves smoothly because of its material nature. A video comparing the geodesic vortex boundary with the Nash edge is available (video 3: <https://goo.gl/7CQ9cu>). The video shows that sometimes

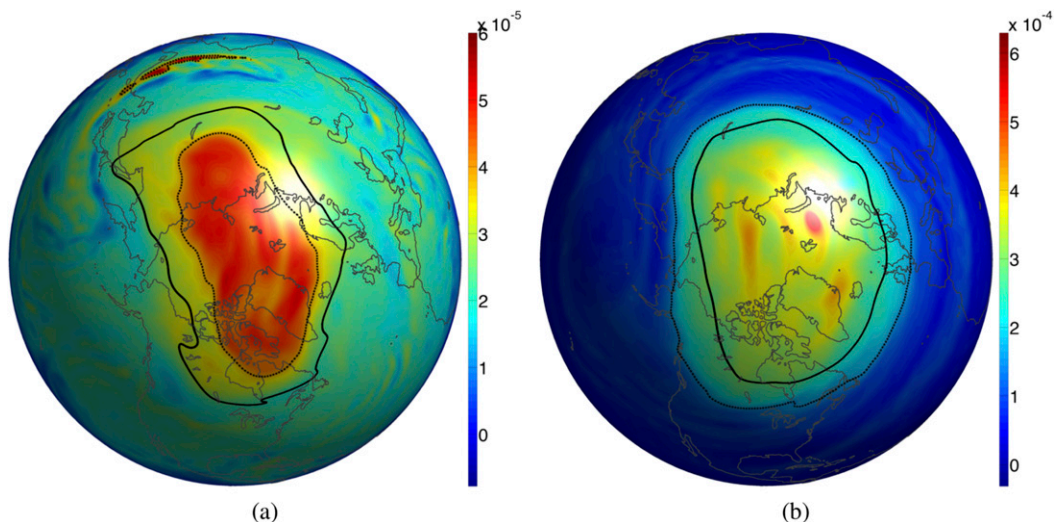


FIG. 7. PV ($\text{K m}^2 \text{kg}^{-1} \text{s}^{-1}$) on the (a) 475- and (b) 700-K isentropic surfaces on 28 Dec 2013. The Nash edge, that is, the PV contour with the highest gradient of PV with respect to the equivalent latitude, is shown by dashed curves; the geodesic vortex boundary is shown by thick black curves. Small pockets of high-PV air are also enclosed by the Nash edge in (a). The evolution of the Nash edge and the geodesic vortex edge during the 10-day time window is available (video 3: <https://goo.gl/7CQ9cu>).

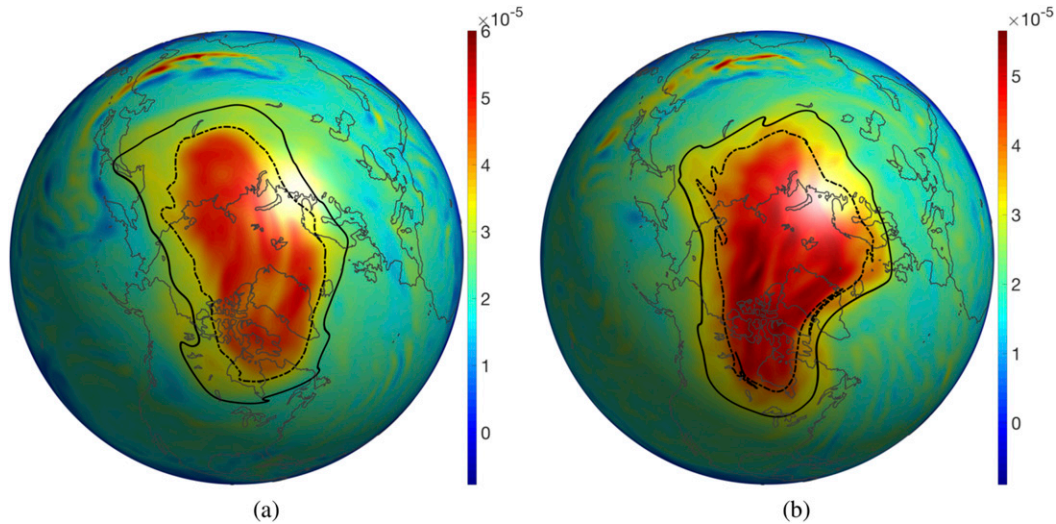


FIG. 8. (a) The dashed line shows the initial position of the minimally stretched PV contour over the time interval 28 Dec 2013–7 Jan 2014 on the 475-K isentropic surface. The solid line and the scalar field show the geodesic polar vortex edge and the PV field at the initial time. (b) Final position of the minimally stretched PV contour and the geodesic vortex edge shown in (a), along with the PV field at the final time.

the jumps in the vortex edge identified by the Nash method are dramatic and include high-value PV arms, which is inconsistent with how the main vortex is envisioned (see introduction).

A video with the three-dimensional evolution of the Nash edge computed over different isentropic surfaces is available (video 4: <https://goo.gl/7CQ9cu>), to be compared with video 1. Video 4 shows substantial jumps in the bounding surface from one time step to another, due to the nonmaterial nature of the vortex boundaries returned by this method. See also Tuck (1994) for the limitations of PV-based methods for identifying the polar vortex edge.

2) MINIMALLY STRETCHING PV CONTOUR METHOD

In this section, we compare the geodesic polar vortex edge with the one obtained using the minimally stretching PV contour (Chen 1994), that is, the PV isoline at the initial time that undergoes minimal material stretching over a preselected time interval. Here, we consider the interval from 28 December 2013 to 7 January 2014 and discretize the PV contours in intervals of $0.5 \times 10^{-6} \text{ m}^2 \text{ s}^{-1} \text{ kg}^{-1} \text{ K}$, as in Chen (1994). Compared with the Nash edge, the minimally stretching PV contour returns a material vortex boundary but its definition is frame dependent.

As an illustration, Fig. 8a shows the initial position of the minimally stretching PV contour (dashed line) on the 475-K isentropic surface, along with the geodesic vortex boundary (solid line) and the PV field. Figure 8b

shows the final positions of the vortex boundaries in Fig. 8a, along with the PV field at the final time.

To quantify material deformations, we have found that the stretching ratio of the minimally stretching PV-based edge (i.e., the ratio of its final and initial lengths) is 1.35, while the stretching ratio of the geodesic edge is $\lambda = 1.04$ [cf. Eq. (7)]. This highlights that the geodesic vortex edge is a larger and more coherent vortex boundary than the minimally stretching PV contour edge.

c. Elliptic LCS and the FLTE field

Backward-time FTLE ridges are popular diagnostics for locating generalized unstable manifolds (Shadden 2011; Yeates et al. 2012). Although the FTLE might incorrectly identify even finite-time generalized stable and unstable manifolds (Haller 2015; Branicki and Wiggins 2010; Karrasch 2015), it is still used as a diagnostic for locating vortex-type structures, believed to be marked by low FTLE values surrounded by FTLE ridges. In addition to all these caveats, out of the numerous FTLE ridges, there is no clear strategy to filter and extract them as parameterized curves.

Figure 9 shows the geodesic vortex edge (black) on 7 January 2014 on two different isentropic levels, along with the corresponding backward-time FTLE fields. On each isentropic surface, the FTLE field has a complex filamentary structure; this complexity increases in the surfaces at lower altitudes. This is because the vertical shear of the stratospheric polar vortex traps synoptic-scale waves in the troposphere while allowing planetary-scale waves to propagate into

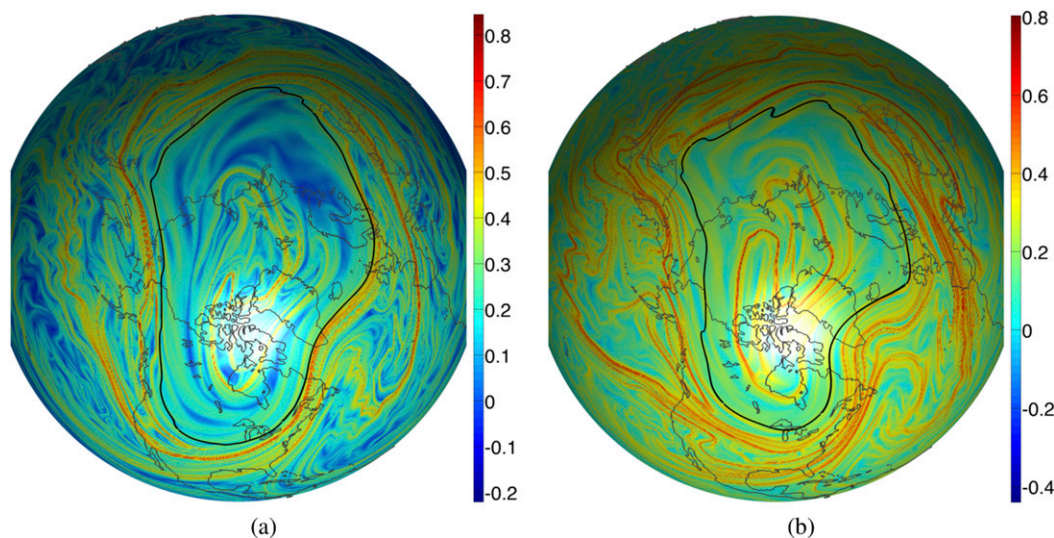


FIG. 9. Positions of geodesic vortex boundaries (thick black curves) on 7 Jan 2014, plotted over the backward-time FTLE field on the (a) 530- and (b) 475-K isentropic surfaces.

the stratosphere. As a result of this mechanism, the stratospheric flow at lower altitude has more power at shorter wavelengths. Figure 9a shows the results at the 530-K isentropic surface and Fig. 9b at the 475-K isentropic surface, which is at a lower altitude; both panels show numerous strands of high FTLE values emanating toward the equator.

Figure 9 shows that parts of some FTLE ridges approximate the optimal location of the polar vortex boundary, but there is no clearly defined, single FTLE ridge marking this boundary. Analogous results would be obtained by computing FTLE over non-Euclidean manifolds with the method developed by Lekien and Ross (2010) [cf. Fig. 9 in Lekien and Ross (2010)]. Similar conclusions about the forward-time FSLE had been made in Joseph and Legras (2002), with the corresponding FSLE ridges penetrating the surf zone and forming a highly mixed stochastic layer rather than identifying a coherent transport barrier. In contrast, the geodesic vortex boundary returns the exact location of the coherent vortex edge, as we demonstrated above by actual material advection.

d. Elliptic LCS and the ozone concentration field

The location and shape of the geodesic vortex edge is consistent with the ozone concentration (cf. Fig. 10), in agreement with the chemical composition expected within the main vortex. Here, we use the ozone concentration from ERA-Interim (Dee et al. 2011), which gives a qualitative representation of the real ozone concentration in the stratosphere. See Dee et al. (2011) for a detailed description of the limitations of this dataset. Ozone

concentration behaves approximately like a passive tracer in the stratosphere over several weeks (Andrews et al. 1987) and, thus, evolves with the vortex. Ozone hole formation is anticorrelated to the planetary wave activity (Bodeker and Scourfield 1995; Shindell et al. 1997) and, thus, depends on the strength of the meridional transport barrier enclosing the polar vortex. For example, it has been shown that the polar night jet, a barrier to stratospheric meridional transport of passive tracers such as ozone, accounts for the sharp boundary of the Antarctic ozone hole (Rypina et al. 2006). Bowman (1996) showed that the mixing barrier in the Antarctic polar vortex depends on the relationship between the speed of the jet and phase speed of the existing Rossby wave. Despite the lower subsistence of the Arctic vortex compared to the Antarctic vortex (Vaugh and Randel 1999), the geodesic vortex edge shadows closely the boundary-separating regions of contrasting ozone concentrations over the time window we analyze at every isentropic layer.

As an illustrative example, Figs. 10a and 10b show the vortex edge (black) on 7 January 2014 at 850 and 475 K, respectively, along with their corresponding ozone concentrations. Note the relatively lower and higher ozone concentrations in the polar vortex compared with the surrounding air are a result of the Brewer–Dobson circulation (Mohanakumar 2008). In this mechanism, ozone created in the tropical stratosphere is transported poleward in the lower stratosphere.

e. Elliptic LCS and the temperature field

Temperature does not behave like a passive tracer on isentropic surfaces; hence, it is not expected to advect

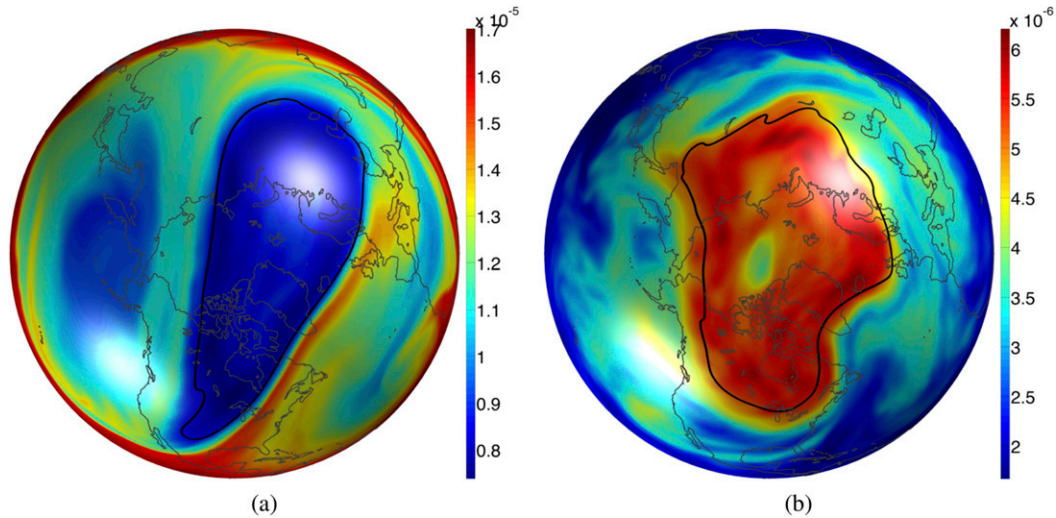


FIG. 10. Nearby sharp contrast in the ozone concentration is observed along the geodesic vortex boundary of each isentropic surface. Shown here are the ozone mass mixing ratios (kg kg^{-1}) on the (a) 850- and (b) 475-K isentropic surfaces on 7 Jan 2014.

as air particles. However, curiously, we generally find that geodesic vortex boundaries on isentropic surfaces turn out to match remarkably well with the temperature fields available on isobaric surfaces roughly 10 km lower in altitude. As an illustration, we show that the geodesic boundaries of the 850- and 700-K isentropic surfaces match well with the temperature fields of the 30- and 50-hPa isobaric surfaces (cf. Fig. 11). Note that we use temperature fields on isobaric surfaces available at Kobayashi et al. (2015) because they are not directly available on isentropic surfaces in the ECMWF database.

In Fig. 12, we show the geodesic vortex edge on the 850-K isentropic surface on 7 January 2014, along with the potential vorticity and the temperature fields. Specifically, Fig. 12a shows the geodesic vortex edge (solid line), the Nash edge (dashed line), and the PV field. Figure 12b shows the geodesic vortex edge and the ozone concentration field, and Fig. 12c shows the geodesic vortex edge and the temperature field of the 30-hPa isobaric surface.

Despite their purely kinematic nature, LCSs show a close match with instantaneous temperature and ozone concentration fields, bringing further evidence that the

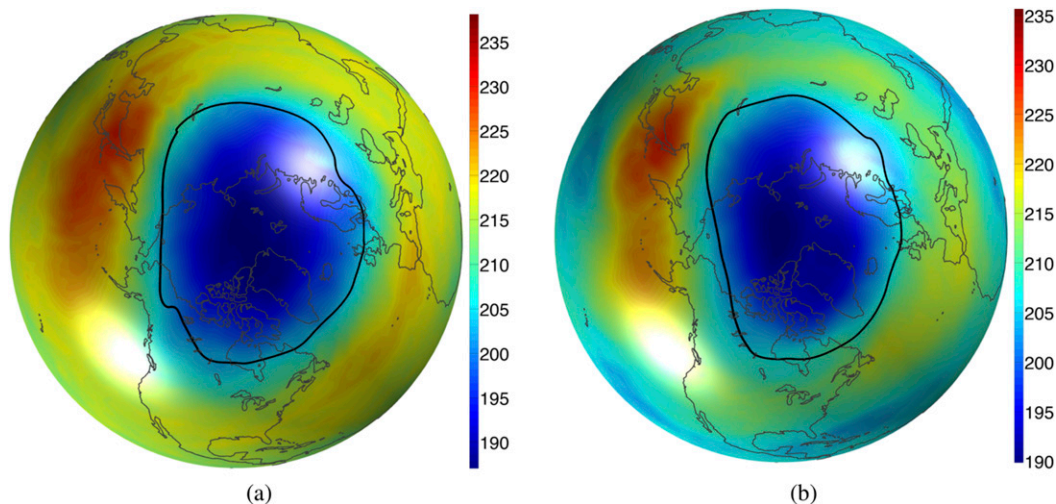


FIG. 11. Temperature fields (K) of (a) 30- and (b) 50-hPa isobaric surfaces (shading) and geodesic vortex boundaries (black lines) on the (a) 850- and (b) 700-K isentropic surfaces on 28 Dec 2013.

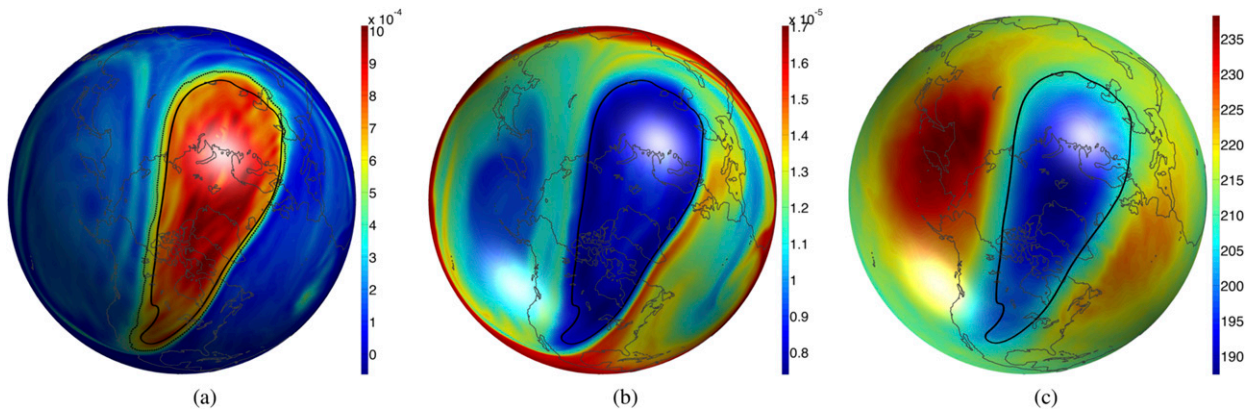


FIG. 12. (a) Geodesic vortex edge (solid line), Nash edge (dashed line), and PV field on 850-K isentropic surface (shading) on 7 Jan 2014. (b) Geodesic vortex edge (black line) and ozone concentration field on 850-K isentropic surface (shading) on 7 Jan 2014. (c) Geodesic vortex edge (black line) on 850-K isentropic surface and temperature field of 30-hPa isobaric surface (shading) on 7 Jan 2014.

geodesic vortex boundary correctly identifies the physically observable polar vortex edge.

5. Conclusions

The two polar vortices are dominant dynamical features of stratospheric circulation. During fall and winter, they exemplify coherent vortical motion, with a delineating transport barrier commonly referred to as the “vortex edge” outside which lies the highly mixed “surf zone.” The interest in the polar vortices has been motivated by the central role they play in the ozone hole formation (World Meteorological Organization 1992; McIntyre 1995), as well as their influence over tropospheric weather (Thompson and Wallace 1998, 2000).

Using the recently developed geodesic theory of Lagrangian coherent structures (Haller 2015; Serra and Haller 2017a), we have computed geodesic vortex boundaries on various isentropic surfaces during late December 2013 and early January 2014, when an exceptional cold wave was recorded in the northeastern United States. Geodesic LCS theory enables us to identify the polar vortex edge as a smooth parameterized material surface. In comparison to other diagnostics used for the vortex edge identification, the geodesic LCS method uniquely identifies a materially optimal (i.e., maximal and nonfilamenting) vortex boundary, dividing the main vortex from the surf zone. We verify this optimality by actual material advection of the geodesic vortex edge and its normal perturbation. Remarkably, we find that even a slightly normally perturbed surface exhibits substantial advective mixing with the tropical air, while the geodesic

edge remains perfectly coherent, conforming to the original idea for a vortex edge. We find that the polar vortex is initially roughly symmetrically placed in late December 2013, while it deforms toward the northeastern coast of the United States in early January 2014, consistent with the severe cold registered over this period.

Isentropic PV was instrumental in realizing the “main vortex surf zone” (McIntyre and Palmer 1984; Jukes and McIntyre 1987; McIntyre and Palmer 1983) distinction in the stratospheric polar vortex. A popular PV-based method posits the vortex edge as the PV contour with the highest PV gradient with respect to equivalent latitude (Nash et al. 1996). We have observed that despite its simplicity, this method sometimes underestimates and sometimes overestimates the extent of the coherent vortex core. Furthermore, because of their Eulerian nature, PV-based methods are inherently suboptimal for material assessments; that is, there is usually a substantial material flux through the Eulerian vortex boundaries they determine. The geodesic LCS theory used here is purely kinematic and, hence, model independent. Not only is it immune to model-dependent fallibility of diagnostics, such as PV, but it is also objective (i.e., frame independent). Despite its kinematic nature, the method renders a vortex edge that closely matches sharp gradients in the temperature field and ozone concentration.

Acknowledgments. We acknowledge helpful discussions with Mohammad Farazmand and Maria Josefina Olascoaga, and Pak Wai Chan for pointing out the source of isobaric surface data.

REFERENCES

- Allen, D., and N. Nakamura, 2001: A seasonal climatology of effective diffusivity in the stratosphere. *J. Geophys. Res.*, **106**, 7917–7935, doi:10.1029/2000JD900717.
- Andrews, D., J. Holton, and C. Leovy, 1987: *Middle Atmosphere Dynamics*. International Geophysics Series, Vol. 40, Academic Press, 489 pp.
- Arnold, V. I., 1973: *Ordinary Differential Equations*. MIT Press, 280 pp.
- Baldwin, M., and J. Holton, 1988: Climatology of the stratospheric polar vortex and planetary wave breaking. *J. Atmos. Sci.*, **45**, 1123–1142, [https://doi.org/10.1175/1520-0469\(1988\)045<1123:COTSPV>2.0.CO;2](https://doi.org/10.1175/1520-0469(1988)045<1123:COTSPV>2.0.CO;2).
- Beron-Vera, F. J., M. G. Brown, M. J. Olascoaga, I. I. Rypina, H. Koçak, and I. A. Udovydchenkov, 2008: Zonal jets as transport barriers in planetary atmospheres. *J. Atmos. Sci.*, **65**, 3316–3326, <https://doi.org/10.1175/2008JAS2579.1>.
- , M. J. Olascoaga, M. G. Brown, H. Koçak, and I. I. Rypina, 2010: Invariant-tori-like Lagrangian coherent structures in geophysical flows. *Chaos*, **20**, 017514, <https://doi.org/10.1063/1.3271342>.
- , —, —, and —, 2012: Zonal jets as meridional transport barriers in the subtropical and polar lower stratosphere. *J. Atmos. Sci.*, **69**, 753–767, <https://doi.org/10.1175/JAS-D-11-084.1>.
- , Y. Wang, M. J. Olascoaga, G. J. Goni, and G. Haller, 2013: Objective detection of oceanic eddies and the Agulhas leakage. *J. Phys. Oceanogr.*, **43**, 1426–1438, doi:10.1175/JPO-D-12-0171.1.
- Bodeker, G., and M. Scourfield, 1995: Planetary waves in total ozone and their relation to Antarctic ozone depletion. *Geophys. Res. Lett.*, **22**, 2949–2952, doi:10.1029/95GL01778.
- Bowman, K., 1993: Large-scale isentropic mixing properties of the Antarctic polar vortex from analyzed winds. *J. Geophys. Res.*, **98**, 23 013–23 027, doi:10.1029/93JD02599.
- , 1996: Rossby wave phase speeds and mixing barriers in the stratosphere. Part I: Observations. *J. Atmos. Sci.*, **53**, 905–916, [https://doi.org/10.1175/1520-0469\(1996\)053<0905:RWPSAM>2.0.CO;2](https://doi.org/10.1175/1520-0469(1996)053<0905:RWPSAM>2.0.CO;2).
- Branicki, M., and S. Wiggins, 2010: Finite-time Lagrangian transport analysis: Stable and unstable manifolds of hyperbolic trajectories and finite-time Lyapunov exponents. *Nonlinear Processes Geophys.*, **17**, 1–36, <https://doi.org/10.5194/npg-17-1-2010>.
- Butchart, N., and E. Remsberg, 1986: The area of the stratospheric polar vortex as a diagnostic for tracer transport on an isentropic surface. *J. Atmos. Sci.*, **43**, 1319–1339, [https://doi.org/10.1175/1520-0469\(1986\)043<1319:TAOTSP>2.0.CO;2](https://doi.org/10.1175/1520-0469(1986)043<1319:TAOTSP>2.0.CO;2).
- Chen, P., 1994: The permeability of the Antarctic vortex edge. *J. Geophys. Res.*, **99**, 20 563–20 571, doi:10.1029/94JD01754.
- Dee, D., and Coauthors, 2011: The ERA-Interim reanalysis: Configuration and performance of the data assimilation system. *Quart. J. Roy. Meteor. Soc.*, **137**, 553–597, <https://doi.org/10.1002/qj.828>.
- De La Cámara, A., C. Mechoso, K. Ide, R. Walterscheid, and G. Schubert, 2010: Polar night vortex breakdown and large-scale stirring in the southern stratosphere. *Climate Dyn.*, **35**, 965–975, doi:10.1007/s00382-009-0632-6.
- , A. Mancho, K. Ide, E. Serrano, and C. Mechoso, 2012: Routes of transport across the Antarctic polar vortex in the southern spring. *J. Atmos. Sci.*, **69**, 741–752, <https://doi.org/10.1175/JAS-D-11-0142.1>.
- Farazmand, M., D. Blazevski, and G. Haller, 2014: Shearless transport barriers in unsteady two-dimensional flows and maps. *Physica D*, **278–279**, 44–57, doi:10.1016/j.physd.2014.03.008.
- Hadjighasem, A., and G. Haller, 2016: Geodesic transport barriers in Jupiter’s atmosphere: A video-based analysis. *SIAM Rev.*, **58**, 69–89, doi:10.1137/140983665.
- Haller, G., 2001: Distinguished material surfaces and coherent structures in three-dimensional fluid flows. *Physica D*, **149**, 248–277, doi:10.1016/S0167-2789(00)00199-8.
- , 2002: Lagrangian coherent structures from approximate velocity data. *Phys. Fluids*, **14**, 1851–1861, doi:10.1063/1.1477449.
- , 2015: Lagrangian coherent structures. *Annu. Rev. Fluid Mech.*, **47**, 137–162, doi:10.1146/annurev-fluid-010313-141322.
- , and F. Beron-Vera, 2013: Coherent Lagrangian vortices: The black holes of turbulence. *J. Fluid Mech.*, **731**, R4, doi:10.1017/jfm.2013.391.
- Hannachi, A., D. Mitchell, L. Gray, and A. Charlton-Perez, 2011: On the use of geometric moments to examine the continuum of sudden stratospheric warmings. *J. Atmos. Sci.*, **68**, 657–674, <https://doi.org/10.1175/2010JAS3585.1>.
- Hartmann, D., L. Heidt, M. Loewenstein, J. Podolske, J. Vedder, W. Starr, and S. Strahan, 1989a: Transport into the south polar vortex in early spring. *J. Geophys. Res.*, **94**, 16 779–16 795, doi:10.1029/JD094iD14p16779.
- , and Coauthors, 1989b: Potential vorticity and mixing in the south polar vortex during spring. *J. Geophys. Res.*, **94**, 11 625–11 640, doi:10.1029/JD094iD09p11625.
- Harvey, V. L., C. Randall, and R. Collins, 2015: Chemical definition of the mesospheric polar vortex. *J. Geophys. Res. Atmos.*, **120**, 10 166–10 179, doi:10.1002/2015JD023488.
- Hauchecorne, A., S. Godin, M. Marchand, B. Heese, and C. Souprayen, 2002: Quantification of the transport of chemical constituents from the polar vortex to midlatitudes in the lower stratosphere using the high-resolution advection model MIMOSA and effective diffusivity. *J. Geophys. Res.*, **107**, 8289, doi:10.1029/2001JD000491.
- Haynes, P., and E. Shuckburgh, 2000: Effective diffusivity as a diagnostic of atmospheric transport: I. Stratosphere. *J. Geophys. Res.*, **105**, 22 777–22 794, <https://doi.org/10.1029/2000JD900093>.
- Hood, L., and B. Soukharev, 2005: Interannual variations of total ozone at northern midlatitudes correlated with stratospheric EP flux and potential vorticity. *J. Atmos. Sci.*, **62**, 3724–3740, <https://doi.org/10.1175/JAS3559.1>.
- Huck, P., A. McDonald, G. Bodeker, and H. Struthers, 2005: Interannual variability in Antarctic ozone depletion controlled by planetary waves and polar temperature. *Geophys. Res. Lett.*, **32**, L13819, doi:10.1029/2005GL022943.
- Joseph, B., and B. Legras, 2002: Relation between kinematic boundaries, stirring, and barriers for the Antarctic polar vortex. *J. Atmos. Sci.*, **59**, 1198–1212, [https://doi.org/10.1175/1520-0469\(2002\)059<1198:RBKBSA>2.0.CO;2](https://doi.org/10.1175/1520-0469(2002)059<1198:RBKBSA>2.0.CO;2).
- Juckes, M., and M. McIntyre, 1987: A high-resolution one-layer model of breaking planetary waves in the stratosphere. *Nature*, **328**, 590–596, doi:10.1038/328590a0.
- Karrasch, D., 2015: Attracting Lagrangian coherent structures on Riemannian manifolds. *Chaos*, **25**, 087411, <https://doi.org/10.1063/1.4928451>.
- , F. Huhn, and G. Haller, 2015: Automated detection of coherent Lagrangian vortices in two-dimensional unsteady flows. *Proc. Roy. Soc. London*, **471A**, 20140639, <https://doi.org/10.1098/rspa.2014.0639>.
- Kobayashi, S., and Coauthors, 2015: The JRA-55 reanalysis: General specifications and basic characteristics. *J. Meteor. Soc. Japan*, **93**, 5–48, <https://doi.org/10.2151/jmsj.2015-001>

- Koh, T., and B. Legras, 2002: Hyperbolic lines and the stratospheric polar vortex. *Chaos*, **12**, 382–394, doi:10.1063/1.1480442.
- Krueger, A., M. Schoeberl, B. Gary, J. Margitan, K. Chan, M. Loewenstein, and J. Podolske, 1989: A chemical definition of the boundary of the Antarctic ozone hole. *J. Geophys. Res.*, **94**, 11 437–11 448, <https://doi.org/10.1029/JD094iD09p11437>.
- Krützmann, N., A. McDonald, and S. George, 2008: Identification of mixing barriers in chemistry-climate model simulations using Rényi entropy. *Geophys. Res. Lett.*, **35**, L06806, doi:10.1029/2007GL032829.
- Lekien, F., and S. Ross, 2010: The computation of finite-time Lyapunov exponents on unstructured meshes and for non-Euclidean manifolds. *Chaos*, **20**, 017505, <https://doi.org/10.1063/1.3278516>.
- Leovy, C., C.-R. Sun, M. H. Hitchman, E. E. Remsberg, J. M. Russell III, L. L. Gordley, J. C. Gille, and L. V. Lyjak, 1985: Transport of ozone in the middle stratosphere: Evidence for planetary wave breaking. *J. Atmos. Sci.*, **42**, 230–244, [https://doi.org/10.1175/1520-0469\(1985\)042<0230:TOOITM>2.0.CO;2](https://doi.org/10.1175/1520-0469(1985)042<0230:TOOITM>2.0.CO;2).
- Loewenstein, M., J. Podolske, K. Chan, and S. Strahan, 1989: Nitrous oxide as a dynamical tracer in the 1987 Airborne Antarctic Ozone Experiment. *J. Geophys. Res.*, **94**, 11 589–11 598, doi:10.1029/JD094iD09p11589.
- Madrid, J., and A. Mancho, 2009: Distinguished trajectories in time dependent vector fields. *Chaos*, **19**, 013111, <https://doi.org/10.1063/1.3056050>.
- McDonald, A. J., and M. Smith, 2013: A technique to identify vortex air using carbon monoxide observations. *J. Geophys. Res. Atmos.*, **118**, 12 719–12 733, doi:10.1002/2012JD019257.
- McIntyre, M. E., 1989: On the Antarctic ozone hole. *J. Atmos. Terr. Phys.*, **51**, 29–43, doi:10.1016/0021-9169(89)90071-8.
- , 1995: The stratospheric polar vortex and sub-vortex: Fluid dynamics and midlatitude ozone loss. *Philos. Trans. Roy. Soc. London*, **352A**, 227–240, <https://doi.org/10.1098/rsta.1995.0066>.
- , and T. N. Palmer, 1983: Breaking planetary waves in the stratosphere. *Nature*, **305**, 593–600, doi:10.1038/305593a0.
- , and —, 1984: The ‘surf zone’ in the stratosphere. *J. Atmos. Terr. Phys.*, **46**, 825–849, doi:10.1016/0021-9169(84)90063-1.
- Mitchell, D., L. Gray, J. Anstey, M. Baldwin, and A. Charlton-Perez, 2013: The influence of stratospheric vortex displacements and splits on surface climate. *J. Climate*, **26**, 2668–2682, doi:10.1175/JCLI-D-12-00030.1.
- Mizuta, R., and S. Yoden, 2001: Chaotic mixing and transport barriers in an idealized stratospheric polar vortex. *J. Atmos. Sci.*, **58**, 2616–2629, [https://doi.org/10.1175/1520-0469\(2001\)058<2616:CMATBI>2.0.CO;2](https://doi.org/10.1175/1520-0469(2001)058<2616:CMATBI>2.0.CO;2).
- Mohanakumar, K., 2008: *Stratosphere Troposphere Interactions: An Introduction*. Springer, 416 pp.
- Morris, G., and Coauthors, 1995: Trajectory mapping and applications to data from the Upper Atmosphere Research Satellite. *J. Geophys. Res.*, **100**, 16 491–16 505, doi:10.1029/95JD01072.
- , J. Gleason, J. Russell, M. Schoeberl, and M. McCormick, 2002: A comparison of HALOE V19 with SAGE II V6.00 ozone observations using trajectory mapping. *J. Geophys. Res.*, **107**, 4177, doi:10.1029/2001JD000847.
- Nakamura, N., 1996: Two-dimensional mixing, edge formation, and permeability diagnosed in an area coordinate. *J. Atmos. Sci.*, **53**, 1524–1537, [https://doi.org/10.1175/1520-0469\(1996\)053<1524:TDMEFA>2.0.CO;2](https://doi.org/10.1175/1520-0469(1996)053<1524:TDMEFA>2.0.CO;2).
- Nash, E. R., P. A. Newman, J. E. Rosenfield, and M. R. Schoeberl, 1996: An objective determination of the polar vortex using Ertel’s potential vorticity. *J. Geophys. Res.*, **101**, 9471–9478, <https://doi.org/10.1029/96JD00066>.
- Norton, W., 1994: Breaking Rossby waves in a model stratosphere diagnosed by a vortex-following coordinate system and a technique for advecting material contours. *J. Atmos. Sci.*, **51**, 654–673, [https://doi.org/10.1175/1520-0469\(1994\)051<0654:BRWIAM>2.0.CO;2](https://doi.org/10.1175/1520-0469(1994)051<0654:BRWIAM>2.0.CO;2).
- Olascoaga, M. J., M. G. Brown, F. J. Beron-Vera, and H. Koçak, 2012: Brief communication “Stratospheric winds, transport barriers and the 2011 Arctic ozone hole.” *Nonlinear Processes Geophys.*, **19**, 687–692, doi:10.5194/npg-19-687-2012.
- Russell, J., A. Tuck, L. Gordley, J. Park, S. Drayson, J. Harries, R. Cicerone, and P. Crutzen, 1993: HALOE Antarctic observations in the spring of 1991. *Geophys. Res. Lett.*, **20**, 719–722, doi:10.1029/93GL00497.
- Rypina, I. I., M. G. Brown, F. J. Beron-Vera, H. Koçak, M. J. Olascoaga, and I. A. Udovydchenkov, 2006: On the Lagrangian dynamics of atmospheric zonal jets and the permeability of the stratospheric polar vortex. *J. Atmos. Sci.*, **64**, 3595–3610, <https://doi.org/10.1175/JAS4036.1>.
- Santitissadeekorn, N., G. Froyland, and A. Monahan, 2010: Optimally coherent sets in geophysical flows: A transfer-operator approach to delimiting the stratospheric polar vortex. *Phys. Rev.*, **82E**, 056311, <https://doi.org/10.1103/PhysRevE.82.056311>.
- Schoeberl, M. R., and D. L. Hartmann, 1991: The dynamics of the stratospheric polar vortex and its relation to springtime ozone depletions. *Science*, **251**, 46–52, doi:10.1126/science.251.4989.46.
- , and Coauthors, 1989: Reconstruction of the constituent distribution and trends in the Antarctic polar vortex from ER-2 flight observations. *J. Geophys. Res.*, **94**, 16 815–16 845, doi:10.1029/JD094iD14p16815.
- , L. Lait, P. Newman, and J. Rosenfield, 1992: The structure of the polar vortex. *J. Geophys. Res.*, **97**, 7859–7882, doi:10.1029/91JD02168.
- Serra, M., and G. Haller, 2017a: Efficient computation of null geodesics with applications to coherent vortex detection. *Proc. Roy. Soc. London*, **473A**, 20160807, <https://doi.org/10.1098/rspa.2016.0807>.
- , and —, 2017b: Forecasting long-lived Lagrangian vortices from their objective Eulerian footprints. *J. Fluid Mech.*, **813**, 436–457, doi:10.1017/jfm.2016.865.
- Shadden, S., 2011: Lagrangian coherent structures. *Transport and Mixing in Laminar Flows: From Microfluidics to Oceanic Currents*, R. Grigoriev, Ed., Wiley, 59–89.
- Shepherd, T., 2007: Transport in the middle atmosphere. *J. Meteor. Soc. Japan*, **85**, 165–191, <https://doi.org/10.2151/jmsj.85B.165>.
- Shindell, D., S. Wong, and D. Rind, 1997: Interannual variability of the Antarctic ozone hole in a GCM. Part I: The influence of tropospheric wave variability. *J. Atmos. Sci.*, **54**, 2308–2319, [https://doi.org/10.1175/1520-0469\(1997\)054<2308:IVOTAO>2.0.CO;2](https://doi.org/10.1175/1520-0469(1997)054<2308:IVOTAO>2.0.CO;2).
- Smith, M., and A. McDonald, 2014: A quantitative measure of polar vortex strength using the function *M*. *J. Geophys. Res. Atmos.*, **119**, 5966–5985, doi:10.1002/2013JD020572.
- Sparling, L., 2000: Statistical perspectives on stratospheric transport. *Rev. Geophys.*, **38**, 417–436, doi:10.1029/1999RG000070.
- Steinhorst, H., P. Konopka, G. Günther, and R. Müller, 2005: How permeable is the edge of the Arctic vortex: Model studies of winter 1999–2000. *J. Geophys. Res.*, **110**, D06105, doi:10.1029/2004JD005268.

- Thompson, D., and J. Wallace, 1998: The Arctic Oscillation signature in the wintertime geopotential height and temperature fields. *Geophys. Res. Lett.*, **25**, 1297–1300, doi:10.1029/98GL00950.
- , and —, 2000: Annular modes in the extratropical circulation. Part I: Month-to-month variability. *J. Climate*, **13**, 1000–1016, doi:10.1175/1520-0442(2000)013<1000:AMITEC>2.0.CO;2.
- Truesdell, C., and W. Noll, 2004: *The Non-Linear Field Theories of Mechanics*. S. S. Antman, Ed., Springer, 579 pp.
- Tuck, F., A., 1994: The use of ECMWF products in stratospheric measurement campaigns. *Proc. Workshop on the Stratosphere and Numerical Weather Prediction*, Reading, United Kingdom, European Centre for Medium-Range Weather Forecasts, 73–105.
- Vallis, G., 2006: *Atmospheric and Oceanic Fluid Dynamics: Fundamentals and Large-Scale Circulation*. Cambridge University Press, 745 pp.
- Waugh, D. N. W., 1997: Elliptical diagnostics of stratospheric polar vortices. *Quart. J. Roy. Meteor. Soc.*, **123**, 1725–1748, <https://doi.org/10.1002/qj.49712354213>.
- , and R. A. Plumb, 1994: Contour advection with surgery: A technique for investigating finescale structure in tracer transport. *J. Atmos. Sci.*, **51**, 530–540, [https://doi.org/10.1175/1520-0469\(1994\)051<0530:CAWSAT>2.0.CO;2](https://doi.org/10.1175/1520-0469(1994)051<0530:CAWSAT>2.0.CO;2).
- , and W. J. Randel, 1999: Climatology of Arctic and Antarctic polar vortices using elliptical diagnostics. *J. Atmos. Sci.*, **56**, 1594–1613, [https://doi.org/10.1175/1520-0469\(1999\)056<1594:COAAP>2.0.CO;2](https://doi.org/10.1175/1520-0469(1999)056<1594:COAAP>2.0.CO;2).
- , A. H. Sobel, and L. M. Polvani, 2016: What is the polar vortex, and how does it influence weather? *Bull. Amer. Meteor. Soc.*, **98**, 37–44, <https://doi.org/10.1175/BAMS-D-15-00212.1>.
- World Meteorological Organization, 1992: Scientific assessment of ozone depletion: 1998. World Meteorological Organization Global Ozone Research and Monitoring Project Rep. 44, 725 pp.
- Yeates, A. R., G. Hornig, and B. T. Welsch, 2012: Lagrangian coherent structures in photospheric flows and their implications for coronal magnetic structure. *Astron. Astrophys.*, **539**, A1, <https://doi.org/10.1051/0004-6361/201118278>.
- Zhang, J., W. Tian, M. Chipperfield, F. Xie, and J. Huang, 2016: Persistent shift of the Arctic polar vortex towards the Eurasian continent in recent decades. *Nat. Climate Change*, **6**, 1094–1099, doi:10.1038/nclimate3136.